Iron Nanoparticles to Catalyze Graphitization of Cellulose for Energy Storage Applications

Lina Maria Romero Millan, Amel Ghogia, Claire White, Ange Nzihou

Iron Nanoparticles to Catalyze Graphitization of Cellulose for Energy Storage Applications

Lina M. Romero Millán, Amel C. Ghogia, Claire E. White, and Ange Nzihou*

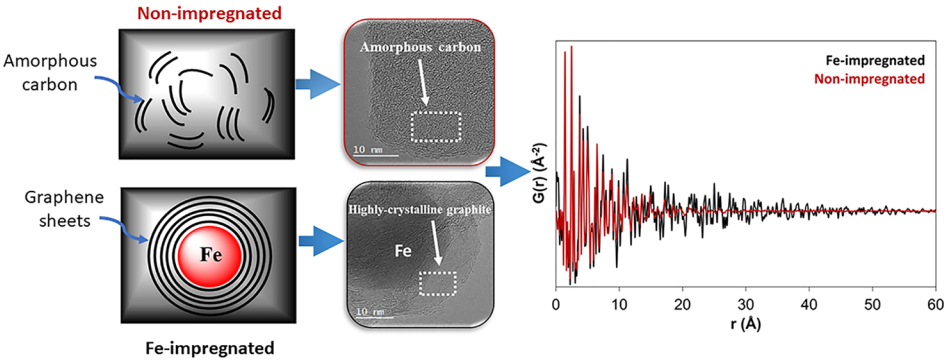

ABSTRACT: The production of highly graphitic carbon from bioresources is an environmentally friendly approach to synthesize graphene for energy storage applications. Iron catalytic graphitization of cellulose, the most abundant biopolymer on earth, is an alternative approach as until now, cellulose has been classified as poorly graphitizable material. In this study, the impact of processing temperature and iron impregnation on the extent of graphitization of the cellulose-derived graphitic carbon nanostructure is uncovered by combining Raman spectroscopy, X-raydiffraction, transmission electron microscopy, and X-ray pair distribution function analysis. Raman spectroscopy is used in an innovative way to describe the evolution of the average graphitic phase size where the ash content misguides the X-ray diffraction analysis. A correlation was established between (i) the in-plane crystallite size L_a and the $I_{D''}/I_G$ first-order ratio, (ii) the out-of-plane L_c crystallite size and the $I_G/I_{tot'}$ second-order ratio, and (iii) the second-order Raman $I_{G'}/I_{tot'}$ ratio and the average number of carbon layers per carbon crystallite. For iron-impregnated cellulose, phase quantification and analysis of the spatial distribution reveal highly crystalline rhombohedral graphite surrounded by a nanocrystalline carbon matrix. We explicitly show that traditionally non-graphitizable carbons can be used to form a graphite-like structure with multilayers of graphene sheets by careful addition of widely available nontoxic metal as catalysts. The study also shows that the impact of the catalyst is much more effective than the temperature in the nanostructure transformation. The proposed approach and the results obtained provide interesting insights that should stimulate further works aimed at extending the knowledge in the field.

INTRODUCTION

Widespread attention has been paid to the development of two-dimensional graphene due to its distinctive and extraordinary properties.[1−3] Owing to these characteristics, graphene is considered a promising material for energy storage applications.[4] In general, graphene synthesis can be performed using top-down and bottom-up methods. In the top-down approach, graphene is derived or exfoliated from graphite to form nanosized graphene sheets.[5,6] In contrast, bottom-up methods involve the growth of graphene from atomic-sized precursors on a support.[7,8] This latter approach often requires sophisticated equipment and strict operating conditions, increasing the production cost in comparison to top-down methods. Considering these restrictions, top-down methods are presently the most common for the production of commercial graphene.

Top-down methods generally use synthetic graphite from fossil sources like coke, pitch, or coal as precursor for graphene synthesis, involving costly and energy-intensive preparation conditions with extremely high temperatures (>2000 °C).[9] Greener methods have been explored that produce graphitic materials with lower environmental impact. For example, some biomass is a sustainable precursor that can be easily converted into a graphitic material using thermochemical decomposition

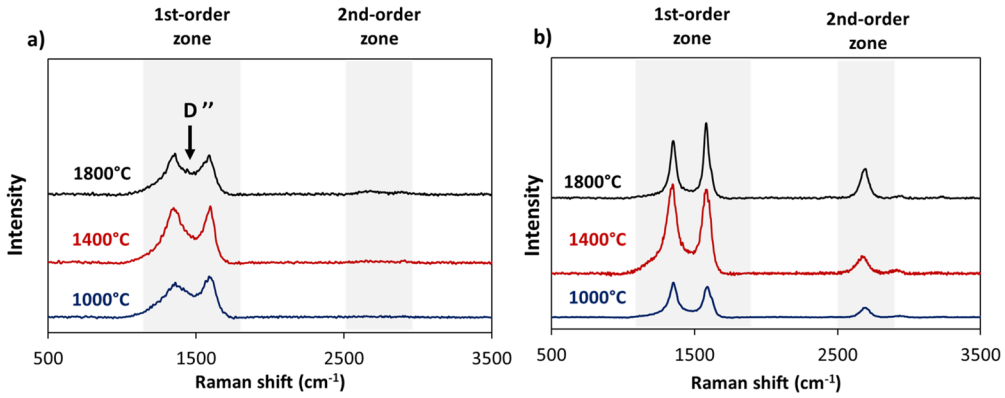

Figure 1. (a) Raman spectra of select graphitic carbons from nonimpregnated microcrystalline cellulose. Only a broad bump is observed for the second-order band of all the analyzed samples. (b) Raman spectra of carbons from iron-impregnated precursors. An evolution of the first- and second-order bands is observed, in contrast to the nonimpregnated samples. The second-order band is characteristic of graphitic materials.

processes.[10] However, cellulose, the main constituent in lignocellulosic biomass and the most abundant source of sustainable carbon, is a non-graphitizable material, and as a consequence, the resulting graphitic carbons may exhibit a randomly oriented carbon structure even after pyrolysis at high temperatures.[11] This characteristic may represent a barrier for the production of graphene, considering that highly ordered graphitic structures are required. Interestingly, different studies have demonstrated that transition metals may catalyze graphitization of other carbon materials.[12] Among them, iron is particularly interesting considering its abundance, relatively nontoxicity, and high catalytic activity toward carbon graphitization compared to other transition metals such as cobalt and nickel.[13−17] Up to now, first-order characteristic bands, especially the D and G peaks of carbonaceous materials, are widely used in the literature to describe the structure evolution of different carbon materials.[10,12,17] Generally, the D band is associated with the presence of defects in the graphitic structure (e.g., crystallite boundaries, defective carbon rings, impurities, etc.),[18] while the G band is related to the in-plane vibration of sp^2-hybridized carbon atoms in graphitic materials.[19] The relationship between these peaks has proved to be suitable for studying graphitizable and graphitic materials[20,21] but does not seem appropriate to evaluate the structure evolution of non-graphitizable feedstocks (e.g., cellulose) and the catalyst-enhanced graphitization process.[22,23] In fact, it has been reported that the lattice region electronically affected by the presence of a defect may be around 2 nm.[24] In this respect, Ferrari and Robertson have shown that the I_D/I_G ratio may decrease during the structural evolution of carbon materials from nanocrystalline graphite to highly ordered graphite. However, they also found that this ratio may decrease with the increase in the structural disorder for carbon materials with a crystallite size below 2 nm.[25] Moreover, other authors have shown that the D band can be even observed in perfectly oriented graphite, near the edges of the carbon crystallites,[26] and has been reported for carbon samples with in-plane crystallite size L_a length as big as 30 nm.[21] Consequently, the developing growth of graphitic zones in non-graphitizable materials by the effect of pyrolysis temperature or the presence of a catalyst may not be directly reflected in the D band, even though other Raman features confirm the graphitization of their carbon structure (i.e., second-order Raman band, $I_{D''}$).

To make affordable highly graphitic carbons from bioresources using a scalable production process, it is necessary to effectively understand and quantify the structural development of these materials during pyrolysis in the presence of iron as catalyst. Several studies in the literature combine Raman spectroscopy and X-ray diffraction (XRD) to provide information about (i) defects in the carbon structure, (ii) stacking of layer, and (iii) average crystallite size for turbostratic carbons with short-range order or highly oriented and ordered materials.[21,27] A recent study showed that the structural development of carbon during iron-catalyzed graphitization can be rationalized by the formation/decomposition of Fe_3C at lower temperature <1000 °C by combining *in situ* X-ray diffraction and X-ray scattering. However, there is a lack of comprehension about the nanostructure of catalyst-enhanced graphitic carbons and its evolution with temperature.[16]

Here, we propose a novel approach to rigorously characterize the carbon structure using second-order Raman bands, and we demonstrate the complementarity of Raman spectroscopy, X-ray scattering, and transmission electron microscopy (TEM) to effectively describe the nanostructure of highly graphitic carbons produced from the catalytic graphitization of cellulose. Cellulose before and after impregnation with iron nitrate solution has been pyrolyzed at different temperatures. From the analysis, we propose a set of empirical correlations to easily assess the average size of the graphitic crystalline domains based on a novel interpretation of the Raman spectra of highly graphitic carbons. We emphasize the validity of the second-order Raman bands, scarcely addressed in the literature, to effectively assess the carbon layer stacking of highly graphitic carbons from a non-graphitizable precursor, extending the applicability of Raman spectroscopy as a versatile tool to quantify the structural development of catalyst-enhanced graphitic carbons. We also reveal the spatial heterogeneity of carbon phase(s) in the iron-containing samples, as assessed using TEM and X-ray pair distribution function (PDF) analysis, which reveal that in pyrolyzed cellulose iron catalyzes the formation of highly crystalline rhombohedral graphite that is dispersed in a nanocrystalline carbon matrix. This work should also open new perspectives in the production and utilization of sustainable graphene materials.

Impact of Pyrolysis Temperature and Iron Content on the Structure of Graphitic Carbon. The structure of the produced highly graphitic carbons was first analyzed using

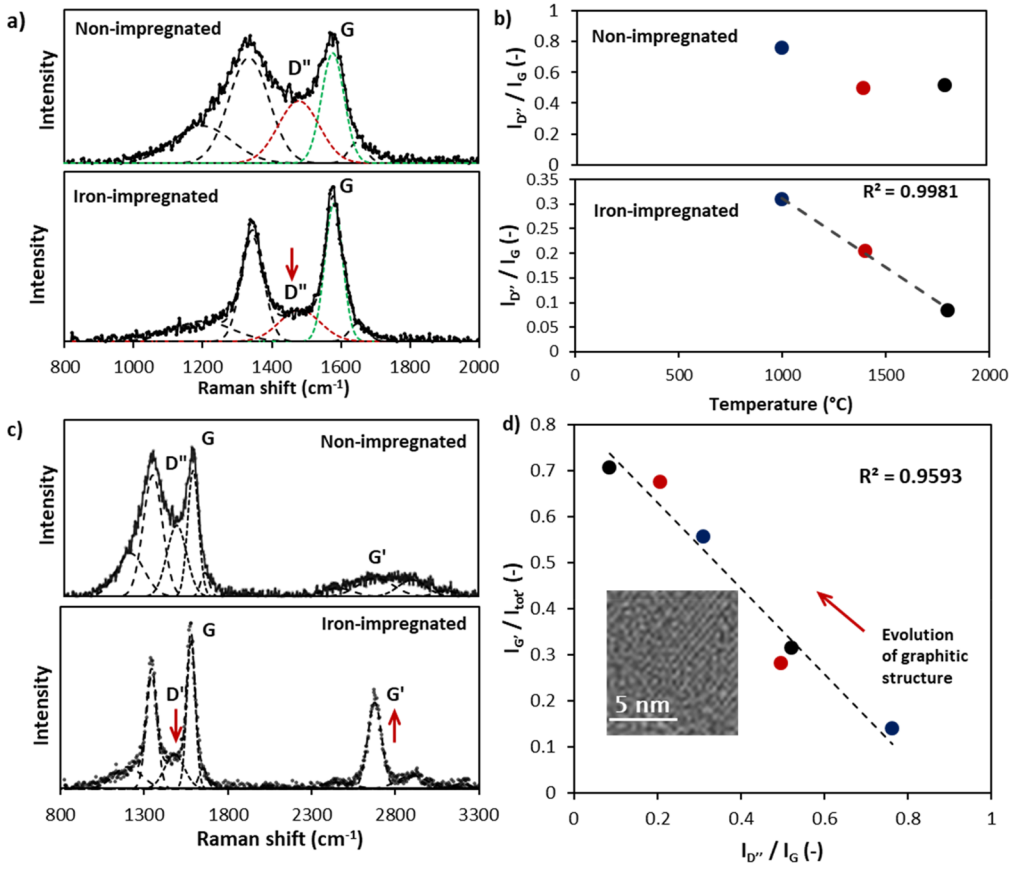

Figure 2. Evolution of structure for non- and iron-impregnated cellulose. (a) First-order Raman bands deconvolution of non- and iron-impregnated cellulose after pyrolysis. (b) Evolution of the first-order $I_{D''}/I_G$ ratio of pyrolyzed cellulose with processing temperature. Iron impregnation is mainly related to a decrease in the D″ feature and consequently in the $I_{D''}/I_G$ ratio. An increase in the G peak is also observed for the iron-impregnated sample. (c) First- and second-order Raman bands deconvolution of non- and iron-impregnated cellulose after pyrolysis. (d) Relationship between the first- and second-order Raman bands of carbon produced from non- and iron-impregnated cellulose and a TEM image which shows the stacking of the graphene layers. A linear correlation is observed between $I_{D''}/I_G$ and $I_{G'}/I_{tot'}$ ratios.

Raman spectroscopy. The normalized Raman spectra of select graphitic carbons at 1000, 1400, and 1800 °C from non- and iron-impregnated microcrystalline cellulose are presented in Figure 1. The spectra of the analyzed samples show the first-order characteristic bands of carbonaceous materials between 1000 and 2000 cm^{-1}, with the peaks D near 1350 cm^{-1} and G near 1580 cm^{-1}, along with intensity D″ near 1500 cm^{-1}, being the most representative bands. In addition to the main D and G bands observed in the Raman spectra of the analyzed graphitic carbons, the impregnated samples also exhibited distinct peaks in the second-order region, between 2500 and 3000 cm^{-1}, while only a broad bump was observed in the nonimpregnated samples.

From the mathematical treatment of the first-order Raman spectra presented in the Methods section, the intensities of the observed bands were analyzed and compared as well as the ratios between them (i.e., I_G/I_{tot}, I_D/I_G, and $I_{D''}/I_G$) to determine the evolution of the carbon structure as a function of pyrolysis temperature and iron impregnation. In the literature, either the ratio of the band heights or the band areas have been used to describe the structure evolution of different carbon materials.[27] However, considering that the band areas may be more sensitive to the discrepancies in the mathematical treatment of the Raman spectra (e.g., fitting functions, number of analyzed bands, bandwidths, etc.), only the band heights have been analyzed in this work.[28]

The experimental results showed that both the increase of pyrolysis temperature and the presence of iron had positive effects on the graphitization of the samples (Figure 2). For both non- and iron-impregnated samples, the temperature increase from 1000 to 1800 °C was associated with a decrease in the $I_{D''}/I_G$ ratio (Figure 2b). In the particular case of nonimpregnated samples, an average reduction of 31% in the $I_{D''}/I_G$ ratio was observed over the analyzed temperature range, suggesting a decrease of sp^2 and sp^3 amorphous structures with the thermal treatment. This effect was accentuated by iron, with an average reduction of 72% in the $I_{D''}/I_G$ ratio, observed for the iron-impregnated samples, suggesting a reduced amount of sp^2 and sp^3 amorphous structures and greater development of graphitic carbon (Figure 2a,b). It is worth noting that the organic composition and the mineral content of the cellulose did not show any significant effect on the graphitization of the samples. In contrast, no significant evolution was observed in the I_G/I_{tot} and I_D/I_G ratios with the temperature increase for nonimpregnated samples and a slight increase of 34% in the I_G/I_{tot} ratio for impregnated samples (see Table S3).

Accordingly, in the first-order region, the $I_{D''}/I_G$ ratio seems to be the most appropriate to describe the evolution of the carbon structure of the analyzed materials. Considering that the D″ band has been generally attributed to the presence of a random mixture of sp^2 and sp^3 amorphous carbons, the

increased degree of structural order of the samples may be related to the decrease of this feature intensity. This impact is scarcely covered in the literature.

As was performed for the first-order bands, the second-order bands were deconvoluted according to the procedure presented in the Methods section, and the relationships between the intensities of the identified bands were analyzed. Particular attention was given to the ratio $I_{G'}/I_{tot'}$ because the G' peak around 2700 cm^{-1} is characteristic of graphitic materials and corresponds to the second-order Raman band of crystalline graphite.[26] The appearance of the G′ peak confirms the presence of highly oriented graphitic structures in the impregnated samples and, thus, the positive impact of iron impregnation on the carbon structure evolution. From the comparison of the first- and second-order Raman bands of all the analyzed samples, a linear relationship was found between the $I_{D''}/I_G$ and $I_{G'}/I_{tot'}$ ratios (Figure 2c,d). Accordingly, the development of graphitic structures is related to a decrease in the $I_{D''}/I_G$ ratio and an increase in the $I_{G'}/I_{tot'}$ ratio. These results confirm that under the analyzed experimental conditions of this investigation the reduction of sp^2 and sp^3 amorphous carbon is associated with the evolution of highly oriented graphitic carbon. Accordingly, the second-order ratio $I_{G'}/I_{tot'}$ may also be a good indicator of the degree of crystallinity for highly graphitic materials from non-graphitizable feedstocks and those processed using the catalyst-enhanced graphitization approach.

Evolution of the Average Crystallite Size of Carbon. In addition to the analysis and comparison of the Raman bands and associated intensity ratios, the evolution of the carbon structure of the pyrolyzed carbon materials may also be described by the carbon crystallite size.[1] The crystallite lattice parameters include the height of the organized stacking of carbon layers L_c, the lateral extension of the graphene sheets L_a, and the average spacing between the layers d_{002}. In this regard, the graphitization of the carbon matrix of the samples should be related to an increase in their carbon crystallite size. X-ray diffraction has been extensively used to characterize the structure of carbon materials and determine their apparent crystallite dimensions. As presented in the Methods section, the L_c and L_a lattice parameters can be deduced using the Debye−Scherrer equation, while the d_{002} distance can be calculated from Bragg's law. The X-ray diffraction results obtained for the samples are presented in Figure 3a,b.

The X-ray diffraction analysis of the produced carbons confirmed the positive effect of the pyrolysis temperature, and particularly of the iron impregnation, on the graphitization of the carbon. It can be observed from Figure 3a that nonimpregnated samples are amorphous/nanocrystalline, showing broad (002) and (10) carbon peaks, with no significant evolution with the temperature increase. Only a slight structural improvement is suggested from the calculated L_c and L_a values. In particular, the temperature rises from 1000 to 1800 °C was related to an increase in the average crystallite size from 0.9 to 1.1 nm for L_c and from 2.9 to 3.9 nm for L_a.

In contrast, the shape of the X-ray diffractograms noticeably changes for iron-impregnated samples (Figure 3b), showing sharp carbon peaks along with those attributed to the iron-containing phases. This confirms the significant impact of iron in enhancing the graphitization of carbon during pyrolysis. From 1000 to 1800 °C the average crystallite size of the samples increased from 4.7 to 6.4 nm for L_c and from 5.4 to 7.2 nm for L_a. From these results, it is clear that the effect of iron

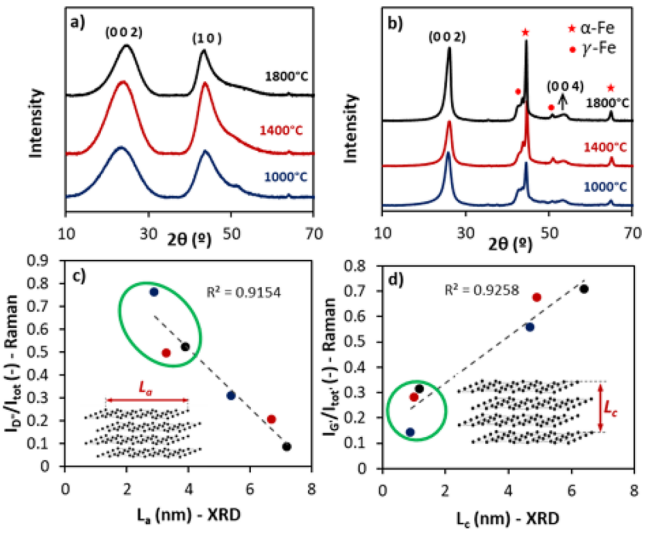

Figure 3. X-ray diffraction (XRD) patterns of graphitic carbon pyrolyzed at 1000, 1400, and 1800 °C: (a) graphitic carbon from nonimpregnated cellulose; (b) graphitic carbon from iron-impregnated cellulose. (∗) α-Fe (ferrite), (●) γ-Fe (austenite), and indices (002), (10), and (004) are noted for the carbon peaks based on the crystal structure of graphite. (c) Relationship between the Raman $I_{G'}/I_{tot'}$ ratio and the calculated L_c crystallite size of the analyzed graphitic carbon. (d) Relationship between the Raman $I_{D''}/I_G$ ratio and the calculated L_a crystallite size of the analyzed graphitic carbons. In both (c) and (d), the samples from nonimpregnated precursors are circled in green. The crystallite size values were calculated from XRD diffractograms.

impregnation in carbon graphitization is much stronger than that of the temperature.

To better understand the evolution of carbon structure, the complementarity between X-ray diffraction and Raman spectroscopy to analyze the structure of nongraphitizable and catalyst-enhanced graphitic carbons was further explored in this study. More specifically, it was observed that the evolution of the carbon crystallite size, calculated from XRD analysis is inversely proportional to the first-order $I_{D''}/I_G$ ratio and proportional to the second-order Raman $I_{G'}/I_{tot'}$ ratio (Figures 3c and 3d, respectively). The observed relationships suggest that Raman spectroscopy could also be used to give insight into the average crystallite size of catalyst-enhanced graphitic carbons. Several authors have already proposed the use of Raman to evaluate the crystallite size of highly ordered materials. The reported studies are mainly focused on the evaluation of the in-plane L_a dimension from the first-order D and G Raman bands. Tunistra and Koening were the first to propose the use of the Raman intensity ratio I_D/I_G to calculate the average L_a crystallite size.[29] The validity of this approach was subsequently confirmed by different authors,[30] where crystallite L_a sizes between 2 and 10 nm have been reported using several different Raman excitation energies.[31,32] Similarly, other reported studies have proposed the calculation of L_a from the HWHM (half-width at half-maximum) of the G peak, fitted using a Breit−Wigner−Fano function (BWF).[33] However, it is worth stressing that the existing correlations for L_a have been established based on highly ordered graphitic materials and, as such, should be considered with caution.[27] As already indicated above, we have demonstrated that the I_D/I_G ratio generally used to calculate the L_a crystallite size is not suitable to describe the carbon structure evolution of non-

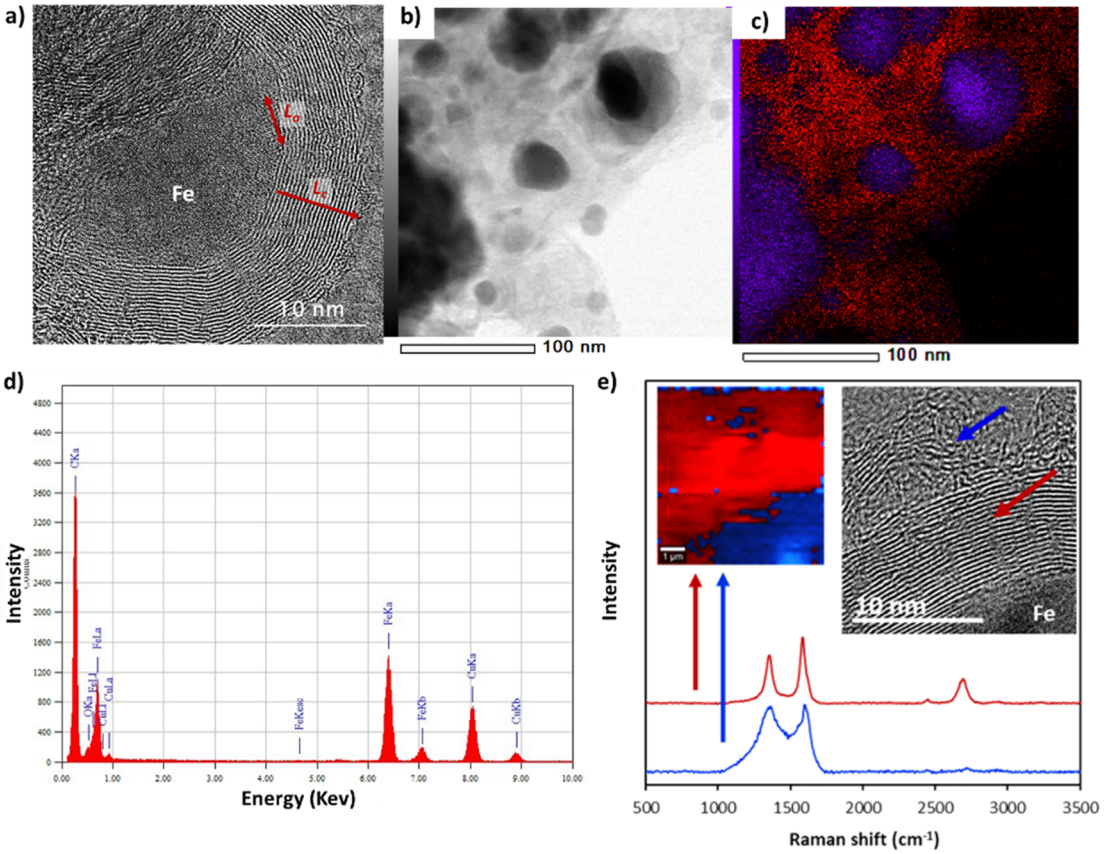

Figure 4. HRTEM image of the produced graphitic carbon nanostructure from iron-impregnated cellulose treated at 1800 °C. (a) The graphitic carbon is formed around the iron nanoparticles. (b) TEM image and (c) TEM-energy dispersive X-ray spectroscopy (EDX) map of the produced carbon showing the dispersion of iron nanoparticles (violet) in the carbon matrix (red). (d) EDX spectrum, where the presence of the copper on the energy-dispersive X-ray (EDX) spectrum comes from the TEM grids that is made of collodion carbon-covered copper film. (e) TEM shows the existence of two domains: in the red arrow, the growth direction of the carbon crystallite size L_a and L_c, and in the blue arrow, the nanocrystalline carbon with short-range order. Raman analysis shows two spectra which correspond to the two different zones (red and blue) on the spatial mapping.

graphitizable or catalyst-induced graphitic carbons and therefore should not be used to estimate the average carbon crystallite size. In contrast, the intensity ratios $I_{G'}/I_{tot'}$ and $I_{D''}/I_G$ are more appropriate to describe these materials.

From the results in Figure 3c, eq 1 was derived to quantitatively describe the linear relationship between the Raman $I_{D''}/I_G$ first-order ratio and the lateral crystallite size L_a calculated from analysis of the (10) diffraction peak using the Scherrer equation (considering the Warren correction).[34] This relationship suggests that the decrease of sp^2 and sp^3 amorphous structures in the samples is associated with an increase in the in-plane lattice size of the carbon crystallite. This is related to the development of highly graphitic structures induced mainly by the iron impregnation of the samples and, to some extent, the pyrolysis temperature. Thus, eq 1 provides an empirical correlation to describe the L_a crystallite size evolution of non-graphitizable materials during the catalytic graphitization process such as cellulose.

$$L_a\ (\text{nm}) = -7.05(I_{D''}/I_G) + 7.69 \quad (1)$$

Concerning the out-of-plane L_c crystallite size, it has been reported that the second-order Raman bands may provide information about the stacking of graphene layers in highly graphitic samples. Malard et al. showed that in the case of carbon AB graphitic stacking analysis of the second-order features allowed the identification of the number of graphene layers, from monolayer to four-layer graphene.[35] In contrast, they pointed out that the identification of the number of layers in nanocrystalline and turbostratic carbons is not as straightforward, considering the random orientation of graphene sheets with respect to each other.

To the best of our knowledge, only one study has attempted to describe the L_c crystallite size of partially disordered graphite from Raman spectroscopy data,[36] where the second-order Raman bands (G') were correlated to the L_c parameter. However, the proposed mathematical treatment to fit these bands was not completely established and may not be suitable to describe the evolution of the catalyst-enhanced graphitization process of carbons. Here, a linear relationship was observed between the $I_{G'}/I_{tot'}$ ratio and the L_c crystallite size determined by the analysis of the (002) diffraction peak using the Scherrer equation. From Figure 3d, it can be seen that higher $I_{G'}/I_{tot'}$ ratios are associated with larger L_c crystallite sizes and, consequently, a greater number of stacked carbon layers. In accordance, an empirical correlation can also be established to describe the average L_c crystallite size of nanocrystalline and catalyst-induced graphitic carbons from their second-order Raman bands.

$$L_c\ (\text{nm}) = 10.03(I_{G'}/I_{tot'}) - 1.30 \quad (2)$$

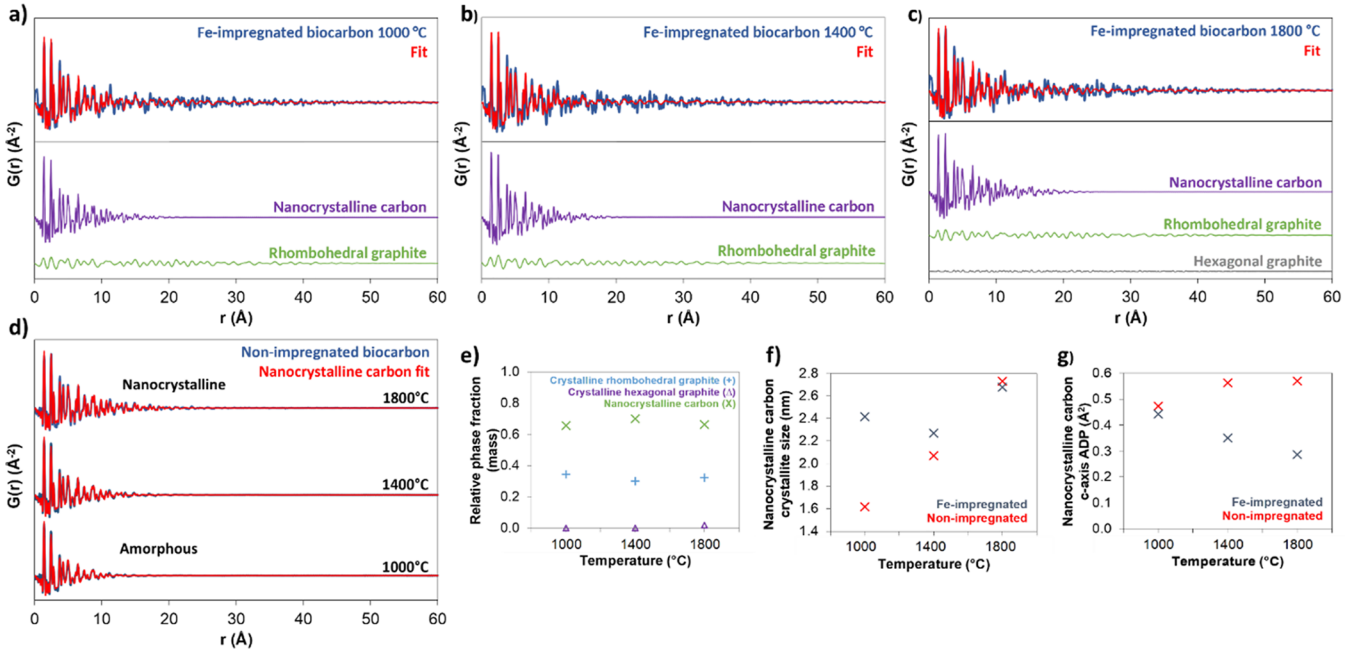

Figure 5. PDFs showing the carbon nanostructure of non- and iron-impregnated cellulose. The carbon nanostructure of iron-impregnated cellulose pyrolyzed at (a) 1000, (b) 1400, and (c) 1800 °C is quantitatively replicated using two (for 1000 and 1400 °C) or three (for 1800 °C) phases. All iron-impregnated samples are found to contain nanocrystalline carbon domains and highly crystalline rhombohedral graphite, while the sample treated at 1800 °C also contains a small amount of highly crystalline hexagonal graphite. (d) The nonimpregnated cellulose samples consist solely of amorphous (1000 °C) or nanocrystalline carbon (1800 °C). (e) Relative phase fraction (by mass) of the carbon phases in the iron-impregnated samples. (f) In-plane crystallite size (i.e., size of graphene sheets) of the non- and iron-impregnated samples obtained from the nanocrystalline carbon crystallite size. (g) *c*-axis atomic displacement parameter (ADP) of nanocrystalline carbon phase. A higher *c*-axis ADP value implies a reduced height of the organized stacking of carbon layers.

With these data, an empirical correlation between the Raman $I_{G'}/I_{tot'}$ ratio and the average number of carbon layers per carbon crystallite is also proposed in this work:

$$n_{avg} = 29.65(I_{G'}/I_{tot'}) - 4.15 \quad (3)$$

These relationships are valid in the L_a size range between 2 and 5 nm and the L_c size range between 1 and 7 nm. Also, they correspond to Raman spectra measured with 532 nm excitation wavelength. From Figure 3c,d, it is worth noting that the crystallite size evolution of the analyzed samples is not the same in the in-plane and out-of-plane directions. In particular, the L_c size increased from an average of 1 nm for nonimpregnated samples to 6 nm for iron-impregnated samples treated at 1300 °C. In contrast, the L_a size evolved to a lesser degree from an average of 3 nm for nonimpregnated samples to around 5 nm for the iron-impregnated samples. These results may be related to the non-graphitizable nature of the cellulose and can be explained by the fact that for impregnated samples the iron nanoparticle controls the L_a parameter because the curvature of the particle governs the curvature of the graphene layers (Figure 4a).

From the above analysis involving the different Raman bands and their ability to shed light on the degree of graphitization of cellulose, the empirical correlation proposed in this work for the calculation of the L_a crystallite size is suitable particularly in the case of iron-catalyzed graphitic materials. In the comparison with the correlation of this work, those already existing in the literature established considering only the D and G Raman bands are only applicable for graphitic materials.[33]

The process of iron catalytic graphitization has been generally described as a dissolution−precipitation mechanism followed by particle growth, where the carbon precursor dissolves in the iron droplets during pyrolysis and subsequently precipitates as graphite during cooling.[12,37,38] This results in the formation of graphitic zones around the iron nanoparticles. As presented in Figure 3b, XRD analysis confirmed the presence of iron phases in the produced carbons in the form of α-Fe and γ-Fe, while the presence of iron carbides was not identified. Considering that the thermal expansion coefficient of iron is higher than that of graphite (~12 to ~6 × 10^{-6} °C^{-1}, respectively),[39] pyrolysis may cause the nanoparticles to expand and break the graphitic shells, forming also carbon nanoribbons and graphitizing other areas of surrounding carbon.[40]

As observed in Figure 4a, the growth of crystalline carbon takes place with a curved stacking of carbon layers around the metal nanoparticle. This curvature is related to the relatively short size of the average in-plane crystallite size (L_a), despite a large number of stacked carbon layers. This characteristic growth of graphitic structures is representative of iron catalyst-enhanced graphitization[37] and may explain the fact that the existing correlations in the literature are not suitable to describe the carbon structure evolution of the analyzed materials. Figure 4b,c shows the spatial distribution of carbon and iron phases in iron-impregnated samples. The simultaneous presence of carbon and iron phases in iron-impregnated samples was confirmed by EDX analysis (Figure 4d). TEM result in Figure 4e showed that the carbon graphitization around iron nanoparticles produces a nonhomogeneous structure at the nanometer scale, with highly crystalline zones adjacent to regions with reduced degrees of nano-

crystallinity. The red Raman spectrum showing the G′ peak and red zone in the mapping correspond to the highly crystalline zones, while those in blue correspond to nanocrystalline carbon (Figure 4e).

These observations can explain the fact that in the analyzed range of iron concentrations higher concentrations in the raw samples resulted in a greater extent of structural ordering of the carbon materials, attributed to the presence of a higher number of iron particles enhancing the graphitization during pyrolysis.

Similarly, Figure 4e illustrates the heterogeneity of the carbon structure of the samples at the nanometer scale, where two distinct Raman spectra for adjacent regions in the same carbon particle exhibit different degrees of organization. The red zone spectrum corresponds to a well-developed crystalline structure, probably near an iron nanoparticle. In contrast, the blue zone spectrum is characteristic of carbon with a lower degree of nanocrystallinity and thus possesses only short-range order (limited to a couple of nanometers). An example of the presence of these zones in the produced graphitic carbon is presented in the TEM image in the figure inset.

Impact of Iron on Graphitic Carbon Nanostructure. As shown by the X-ray diffractograms, the average crystallite size of cellulose-based carbons increased due to iron impregnation, but specific details on the impact of iron impregnation on the nanostructure of the carbon were not accessible using this technique. X-ray total scattering and subsequent PDF analysis is an ideal technique to elucidate the nanostructure of disordered materials.[41] Figure S2 depicts a typical X-ray PDF data set for temperature-treated iron-impregnated cellulose, where the nanostructure of the carbon has been isolated from that of the iron (see the Methods section for the procedure used to remove non-carbon atom−atom correlations from the X-ray PDF). Figure 5a−c shows the PDFs of the carbons contained in the iron-impregnated samples along with their multiphase least-squares refinement results (refinement details outlined in the Methods section). Refinements of the nonimpregnated carbon X-ray PDFs using the same least-squares approach revealed that the nanostructure of these carbons was amorphous (for 1000 °C) or nanocrystalline (for 1800 °C) with atom−atom correlations out to roughly 1.5−2.5 nm (see Figure 5d).

The anisotropic crystallite size of the nanocrystalline carbon phase was modeled in real space by considering a spherical graphite nanocrystallite where the atom−atom correlations along the *c*-axis (i.e., out-of-plane) were suppressed relative to those in the *a*−*b* plane (i.e., in-plane) via directional-dependent refinement of the atomic displacement parameters (ADPs).[42] As such, the in-plane crystallite size (akin to the L_a parameter) can be estimated from the size of the spherical graphite nanocrystallite, while the out-of-plane dimension is expected to be inversely correlated to the magnitude of the *c*-axis ADP, where a larger *c*-axis ADP value implies a smaller out-of-plane nanocrystallite domain size (similar to the L_c parameter). As seen from Figure 5f, the in-plane crystallite size increases from approximately 1.6 to 2.7 nm for non-impregnated cellulose pyrolyzed at 1000 to 1800 °C, respectively. Comparison with X-ray diffraction results, where L_a increased from 2.9 to 3.9 nm for the same treatment temperature range, reveals that the PDF-derived crystallite size is underestimated, likely attributed to the limitations of applying a spherically shaped crystallite during PDF analysis to represent anisotropic crystallites. Nevertheless, the magnitude of increase from 1000 to 1800 °C (1.1 nm from PDF, 1.0 from XRD) is accurately predicted using PDF analysis.

One major finding of the PDF analysis was the identification and quantification of multiple distinct carbon phases in the iron-impregnated samples. Specifically, in addition to the nanocrystalline carbon phase there were found to be larger crystallites of rhombohedral graphite in all iron-impregnated samples along with crystalline hexagonal graphite for the sample treated at 1800 °C (Figure 5a−c). Interestingly, as seen in Figure 5e, the relative amounts of the phases in the iron-impregnated samples do not change significantly with treatment temperature. Instead, these samples roughly consist of 70 wt % nanocrystalline carbon and 30 wt % crystalline rhombohedral graphite. Hence, conventional X-ray diffraction failed to reveal that two distinct carbon phases were present in the iron-impregnated samples, and additional characterization is required to ascertain these details. In fact, the average crystallite size obtained from X-ray diffraction, and specifically the L_c parameter, does not accurately reflect the complex structural details apparent in the TEM images (Figure 4a) where both highly crystalline zones of graphite are seen to be adjacent to regions with reduced degrees of nanocrystallinity. Nevertheless, X-ray diffraction and quantification of the L_a and L_c parameters can accurately capture the general trend of increased crystallinity with treatment temperature and iron impregnation and thus when combined with Raman spectroscopy is ideal for characterization of relative changes in degree of crystallinity for non-graphitizable biomass.

Iron impregnation not only instigates the formation of highly crystalline rhombohedral graphite, but it also catalyzes an increase of the in-plane crystallite size of the nanocrystalline carbon phase, particularly for the lower treatment temperatures (1000 and 1400 °C) as seen in Figure 5f via comparison of the non- and iron-impregnated samples. As alluded to above, PDF analysis of the nanocrystalline carbon phase underestimates the in-plane crystallite size, and thus the crystallite sizes reported in Figure 5f for the iron-impregnated samples are likely underestimated by about 1 nm. Nevertheless, from Figure 5f it is clear that the disordered carbon phase in all iron-impregnated samples is nanocrystalline as opposed to amorphous, and thus iron impregnation not only catalyzes the formation of highly crystalline graphite at 1000 °C but also increases the degree of ordering of the remaining carbon.

Lastly, PDF analysis may also shed light on the impact of iron impregnation and treatment temperature on the height of the organized stacking of carbon layers in the nanocrystalline carbon phase. Figure 5g reports the ADP value of the nanocrystalline carbon phase, which is expected to be inversely correlation with the number of stacked carbon layers, with a higher ADP corresponding to a smaller region of stacked layers. For the nonimpregnated samples this ADP value slightly increased with higher treatment temperature implying less layers in a coherent stack. However, this contradicts the L_c parameter from X-ray diffraction which slightly increased from 0.9 to 1.1 nm; thus, the PDF-derived ADP values may be less sensitive to changes in dimensions of the stacked layers although Poulain et al. did find a correlation between decreasing L_c parameter and increasing *c*-axis ADP for beech biomass as a function of pyrolysis temperature.[42] Hence, the decrease of ADP values for the iron-impregnated samples is likely indicative of an increase in stacked layers for the nanocrystalline carbon phase in these samples, which shows that both the in-plane and out-of-plane dimensions of the

nanocrystalline carbon phase found in the iron-impregnated samples increased as a function of pyrolysis temperature. It remains to be proven if the in-plane and out-of-plane dimensions of the highly crystalline rhombohedral graphite crystals also increase in size with treatment temperature, although the TEM images in Figure 4 indicate that this may indeed be the case.

This study exemplifies how complementary experimental techniques are required to fully understand the nanostructural details of complex carbon materials. For example, TEM showed the existence of two carbon phases in the iron-impregnated samples, while PDF analysis revealed that the crystal structure of the highly crystalline graphite phase was rhombohedral and provided a rough estimate of the relative phase fraction of the individual carbon phases. Raman spectroscopy, and specifically analysis of the first- and second-order bands, allowed for quantification of the relative degree of graphitization for carbons that are traditionally thought to be non-graphitizable, while its comparison with X-ray diffraction enabled for estimation of the average in-plane and out-of-plane carbon crystallite size. The approaches outlined in this study and associated methods pave the way for future investigations of other complex carbon systems, with the aim to discover routes to instigate graphitization of renewable bioresources that until now have been considered non-graphitizable.

CONCLUSION AND OUTLOOK

Cellulose was used for graphitic carbon production from non- and iron-impregnated samples at different temperatures. A multiscale investigation addressing the bulk, molecular, and atomic scales was used to describe the carbon nanostructure. The combination of Raman spectroscopy and X-ray diffraction revealed that the effect of iron impregnation in carbon graphitization is much stronger than that of temperature. This effect of iron as a catalyst for carbon graphitization was confirmed by high-resolution transmission electron microscopy (HRTEM) and X-ray pair distribution function (PDF) analysis of iron-impregnated cellulose biochar, revealing the existence of highly crystalline graphitic domains (identified as rhombohedral graphite in PDF data) dispersed within a disordered arrangement of short-range stacked carbon layers. Such graphitic domains are absent in the nonimpregnated samples. This behavior can be rationalized by considering that the formation of multilayers graphene with a rhombohedral stacking sequence takes place directly on the iron nanoparticles. Using Raman spectroscopy in an innovative way, correlations allowing to calculate the parameters L_a, L_c, and n_{avg} proposed in this work constitute a new approach to describe and quantify the structure of graphitic materials produced from cellulose because the presence of inorganic features in the X-ray diffractograms could complicate or misguide the analysis of the carbon peaks. In addition to Raman, X-ray diffraction, and HRTEM, X-ray PDF analysis revealed that the amorphous carbon making up the nonimpregnated sample after pyrolysis at 1000 °C is nanocrystalline in the iron-impregnated sample, and thus iron impregnation not only catalyzes the formation of highly crystalline rhombohedral graphite but also an increase ordering of the short-range stacked carbon layers. The assessment of the nanostructure development of catalyst-enhanced graphitic carbons from bioresources is a crucial step to effectively advance the development of methods to produce graphene from sustainable and renewable resources for energy storage applications. Current work is devoted to the investigation of parameters such as the particle size and the shape of the initial cellulose to optimize the graphitization. The thermal, electrical, and mechanical properties of the graphitic matrixes obtained will be investigated and compared with carbon graphitized using other approaches developed in the literature.

METHODS

Biomass Precursor. Microcrystalline cellulose (Sigma-Aldrich, CEL) was used in this study to analyze the graphitization during pyrolysis. Microcrystalline cellulose was impregnated with an iron nitrate solution prepared with $Fe(NO_3)_3{\cdot}9H_2O$ (Sigma-Aldrich, 99% purity). 20 g of cellulose was immersed in 200 mL of a 0.049 M solution under continuous stirring for 6 h. The samples were then filtered and dried at 105 °C for 24 h.

To determine the inorganic composition of the non- and iron-impregnated samples, 50 mg of ground sample was acid digested in closed vessels at 220 °C for 4 h. Acid reagents H_2O_2, HNO_3, HF, and H_3BO_3 were used according to EN 16967. Acid solutions were diluted with demineralized water to 50 mL and analyzed using a HORIBA Jobin Yvol Ultima 2 inductively coupled plasma optical emission spectrometer (ICP-OES). The CHNS composition of the samples was determined using a Themoquest NA 2000 elemental analyzer, and their ash content was calculated according to the standard EN ISO 18122. The inorganic and the CHNS compositions of non- and iron-impregnated carbon after pyrolysis were also determined by the same method described above. The compositions of all samples are summarized in Table S1.

Pyrolysis Experiments. Pyrolysis of the non- and iron-impregnated cellulose was performed in a horizontal laboratory-scale reactor, with an internal diameter of 20 mm, externally heated with an electric furnace. For each experiment, between 0.5 and 1 g of sample was placed inside the reactor using a high-temperature ceramic crucible. The samples were pyrolyzed at 1000, 1400, or 1800 °C with a heating rate of 8 °C/min under a nitrogen atmosphere with a gas flow of 1000 mL/min. The pyrolysis temperature was maintained for 1 h, and then the reactor was cooled to room temperature. Finally, the resulting produced carbon was collected, weighed, and stored for further characterization.

Characterization of Graphitic Carbons Using Raman Spectroscopy. Raman spectroscopy was used to analyze the carbon structure of the prepared samples. For this purpose, the carbon samples were mixed and ground with spectroscopic grade KBr in a weight proportion of 1:100 to prevent the sample from being heated during the acquisition of the Raman spectra. The mixtures were compressed using a 13 mm diameter die to form thin pellets for subsequent analysis. The spectra were acquired using a confocal Raman AFM WITEC Alpha 300AR microscope, using an excitation wavelength of 532 nm in the region between 200 and 4000 cm^{-1}. For each sample, at least three different spectra were collected (analysis surface near 25 μm^2), and the average data were calculated. Curve fitting of the Raman spectra was performed using MagicPlot software.

The first-order region between 800 and 2000 cm^{-1} was fitted using five Raman bands, as usually reported for carbon materials, and is summarized in Table S2.[43] Each band was represented using a Gaussian function, where the initial position was fixed for the iteration procedure according to the values in the table. No width limits were fixed for the Raman shift range of the D and G bands, while a maximum width was set for peaks I, D″, and D′ to avoid interference between these features and the D and G bands (width: 100, 70, and 30 cm^{-1}, respectively). In fact, a very large amplitude of peaks I, D″, and D′ may impact the height and amplitude of the main D and G features, hindering correct analysis of their evolution.

The second-order region between 2000 and 3500 cm^{-1} was fitted using four bands as reported in the literature.[44] For the analyzed samples, a good curve fitting was found using Gaussian functions, with initial positions at 2450 cm^{-1} for the I′ peak, 2700 cm^{-1} for the G′ peak, 2900 cm^{-1} for the D+G peak, and 3100 cm^{-1} for the 2D′ peak.

The general descriptions of the second-order features are also summarized in Table S2. In all cases, the maximum peak width was limited to 100 cm^{-1} to reduce overlapping and consider the contribution of each peak. No limits were fixed regarding the Raman shift range.

Characterization of Graphitic Carbons Using X-ray Diffraction. X-ray diffraction analysis was conducted using a Phillips Panalytical X'pert Pro MPD diffractometer and a Cu Kα radiation source (1.543 Å) with a voltage of 4 kV and a current of 40 mA. The diffraction patterns were collected for powder samples (particle size below 250 μm) between $2\theta = 10°$ and $2\theta = 70°$ with a step of 0.05°.

The structure of the carbon samples was determined from analysis of the X-ray diffraction patterns. Particular attention was given to the width of the carbon bands (002) and (10) which are related to the extent of atomic order of graphite-like carbon in the out-of-plane and in-plane direction, respectively.[45] To determine the carbon structural parameters, the (002) and (10) bands were fitted with HighScore software, using pseudo-Voigt functions. The instrument broadening in XRD analysis was removed in order to have accurate values of the L_c and L_a parameters. Thus, a standard NIST sample (silicon) was analyzed under the same conditions as those of the samples. The pseudo-Voigt functions were also used for standard peaks fitting. Because the Voigt function is a convolution of Gaussian and Lorentzian functions, and the Lorentzian function is the dominant cause of broadening,[46] the correction of the mid-width was performed using the Lorentzian shape (see eq 4).

The sample and standard peak widths at half-maximum were automatically calculated by the software, and these values were used to calculate the corrected peak width (eq 4). Then, this latter was used to calculate the average carbon crystallite domain size.

$$\beta_{size} = \beta_{obs} - \beta_{inst} \tag{4}$$

Here, β_{size} is the corrected peak width at the half-maximum intensity in radians, β_{obs} is the sample peak width at the half-maximum intensity in radians, and β_{inst} is the peak width from instrument broadening at the half-maximum intensity in radians.

Accordingly, the average crystallite size L of the samples and the average distance between carbon layers d_{002} were expressed by the Debye−Scherrer equation (eq 5) and Bragg's law (eq 6), respectively:

$$L = \frac{K\lambda}{\beta_{size} \cos\theta} \tag{5}$$

$$d_{002} = \frac{\lambda}{2 \sin\theta_{002}} \tag{6}$$

where θ is the peak position in radians, λ is the X-ray wavelength in nm, and K is a constant that generally depends on the shape of the crystallite.[47] The calculations were performed with K values of 0.89 for L_c (graphitic planes stacking in the carbon crystallite) and 1.84 for L_a (graphite-like atomic order in the single plane).[48]

Characterization of Graphitic Carbons Using High-Resolution Transmission Electron Microscopy (HRTEM). The structure of the prepared carbons was observed using a JEOL JEM-ARM200F high-resolution transmission electron microscope. The elemental mapping of chemical species at the nanoscale was also performed using the microscope X-ray spectroscopy capability (EDX). Powder samples with particle sizes below 250 μm were dispersed in ethanol and mixed in an ultrasonic bath. The samples were then collected from the surface of the solution and deposited onto carbon support films before analysis.

Characterization of Graphitic Carbons Using X-ray Total Scattering and Pair Distribution Function Analysis. The nanostructure of the prepared graphitic carbons was determined using synchrotron-based X-ray total scattering and pair distribution function (PDF) analysis. Samples were loaded into 1 mm diameter polyimide capillaries and measured on the 11-ID-B beamline at the Advanced Photon Source, Argonne National Laboratory. Samples were measured in transmission geometry using a photon wavelength of 60 keV and a 2D image plate detector. High-resolution X-ray diffraction patterns were obtained using a sample-to-detector distance of ~1000 mm, while X-ray total scattering was performed using a distance of ~180 mm. Data reduction was performed using GSAS-II[49] with CeO_2 as the calibrant to obtain 1D data sets. For the total scattering data, the structure factor and PDF were obtained using the PDFgetX2 software,[50] where a Q_{max} of 21.5 $Å^{-1}$ was used for the sine Fourier transform. Instrument parameters were determined using nickel as the standard and the PDFgui software,[51] where Q_{broad} was found to be 0.0200 $Å^{-1}$ and Q_{damp} to be 0.0375 $Å^{-1}$.

Isolation of the graphitic carbon contributions in the iron-impregnated PDF data sets was performed using a direct subtraction method.[52,53] Preliminary analysis of the high-r component of the PDF data sets (above 50 Å) using the real-space PDF modeling software PDFgui revealed that this region was dominated by contributions from α-Fe (ferrite), and no contributions from γ-Fe (austenite) were identified due to the relatively small amount of the γ-Fe phase (see Figure S1 for high-resolution X-ray diffraction patterns). The simulated X-ray PDF for α-Fe was generated using PDFgui and the iron-impregnated sample treated at 1800 °C, where the lattice parameters were refined over an r range of 50−60 Å together with the isotropic atomic displacement parameter (ADP) and scale factor. Subtraction of α-Fe from the iron-impregnated PDFs (to obtain the carbon contributions) was performed after the α-Fe simulated PDF data set was scaled to match that of the iron-impregnated PDF between 50 and 60 Å.

Identification and quantification of the carbon-based nanostructures found in the non- and iron-impregnated carbons were performed using the PDFgui software over an r range of 1−40 Å. Preliminary analysis revealed that the possible contributions to the graphitic carbon PDFs were from crystalline hexagonal and rhombohedral graphite and a disordered nanocrystalline phase based on hexagonal graphite. An amorphous carbon structure was only found to match the PDF of the nonimpregnated sample pyrolyzed at 1000 °C.[54] The PDFs of the nonimpregnated samples pyrolyzed at 1400 and 1800 were better replicated using a nanocrystalline model. Note that crystallite sizes only below ~8−10 nm could be assessed using the 11-ID-B beamline due to its instrument resolution. Therefore, phases identified as crystalline using PDF analysis in this investigation (i.e., α-Fe and crystalline hexagonal and rhombohedral graphite) will consist of crystallites that are larger than ~8−10 nm, where other characterization techniques are required to determine their exact crystallite size. PDFgui software and a least-squares approach were used for the quantification process. First, crystalline hexagonal and rhombohedral graphite phases were refined against the experimental PDFs of the carbons (iron-impregnated) over an r range of 30−40 Å. For both phases the scale factor, lattice parameters, and isotropic ADP were allowed to refine. Refinement of the crystallite sizes for these phases did not lead to an improved fit. A similar refinement for the nonimpregnated biocarbons was not performed due to the absence of discernible atom−atom correlations over this r range. Second, the nanocrystalline carbon phase (based on structure of hexagonal graphite) was refined over an r range of 1−40 Å. At first the parameters for crystalline hexagonal and rhombohedral graphite were kept fixed during the second stage of refinement. During this stage the following parameters for nanocrystalline carbon were allowed to refine: scale factor, lattice parameters, ADPs (c-axis separate from the a/b-axis), and spherical crystallite size. The separate refinement of c-axis ADP and a/b-axis ADP was necessary due to the inability of PDFgui to refine nonspherical crystallite shapes. By allowing the c-axis ADP to refine to a different value, the out-of-plane atom−atom correlations could be decoupled from the in-plane correlations,[42] where a larger c-axis ADP value implies fewer graphene sheets making up the nanocrystallite domain. Subsequent refinement of all phases occurred together with their delta1 values (which account for in-phase vibration of atoms and the greater intensity of the first few atom−atom correlations). The level of agreement between the simulated and experimental PDF was provided by the R_w value, where a smaller value implies better agreement.

AUTHOR INFORMATION

Corresponding Author

Ange Nzihou − *IMT Mines Albi, RAPSODEE CNRS UMR 5302, Université de Toulouse, F.81013 Cedex 09 Albi, France; School of Engineering and Applied Science, Princeton University, Princeton, New Jersey 08544, United States; Andlinger Center for Energy and the Environment, Princeton University, Princeton, New Jersey 08544, United States;* orcid.org/0000-0002-1547-2567; Phone: +33 (0) 5 63 49 32 22; Email: ange.nzihou@mines-albi.fr, ange.nzihou@princeton.edu

Authors

Lina M. Romero Millán − *IMT Mines Albi, RAPSODEE CNRS UMR 5302, Université de Toulouse, F.81013 Cedex 09 Albi, France*

Amel C. Ghogia − *IMT Mines Albi, RAPSODEE CNRS UMR 5302, Université de Toulouse, F.81013 Cedex 09 Albi, France;* orcid.org/0000-0003-2928-5276

Claire E. White − *School of Engineering and Applied Science, Princeton University, Princeton, New Jersey 08544, United States; Andlinger Center for Energy and the Environment, Princeton University, Princeton, New Jersey 08544, United States;* orcid.org/0000-0002-4800-7960

Author Contributions

A.N. supervised, conceived the subject, and wrote the paper. L.M.R.M. and A.C.G. performed the graphitic biochar production, characterization, collected the data and analysis, and wrote the paper. C.E.W. wrote the paper.

Funding

This work was supported by the French "Investissements d"Avenir" program under the Laboratory of Excellence, LABEX SOLSTICE, ANR-10-LABX-22- 01 grant. This work was also financial supported by the Fulbright Commission in granting Professor Nzihou with a research scholarship at Princeton University.

Notes

The authors declare no competing financial interest.

ACKNOWLEDGMENTS

The authors thank colleagues at RAPSODEE Center-IMT Mines Albi (N. Lyczko), Centre de MicroCaractérisation Raimond Castaing (T. Hungria), and LPCNO (G. Ballon).

REFERENCES

(1) Inagaki, M.; Kang, F.; Toyoda, M.; Konno, H. *Advanced Materials Science and Engineering of Carbon*; Elsevier Inc.: 2014.

(2) Zhu, Y.; Murali, S.; Cai, W.; Li, X.; Suk, J. W.; Potts, J. R.; Ruoff, R. S. Graphene and Graphene Oxide: Synthesis, Properties and Applications. *Adv. Mater.* **2010**, *22*, 3906−3924.

(3) Balandin, A. A. Thermal Properties of Graphene and Nanostructured Carbon Materials. *Nature Materials*; Nature Publishing Group: 2011; pp 569−581.

(4) Ren, S.; Rong, P.; Yu, Q. Preparations, Properties and Applications of Graphene in Functional Devices: A Concise Review. *Ceram. Int.* **2018**, *44* (11), 11940−11955.

(5) Paton, K. R.; Varrla, E.; Backes, C.; Smith, R. J.; Khan, U.; O'Neill, A.; Boland, C.; Lotya, M.; Istrate, O. M.; King, P.; Higgins, T.; Barwich, S.; May, P.; Puczkarski, P.; Ahmed, I.; Moebius, M.; Pettersson, H.; Long, E.; Coelho, J.; O'Brien, S. E.; McGuire, E. K.; Sanchez, B. M.; Duesberg, G. S.; McEvoy, N.; Pennycook, T. J.; Downing, C.; Crossley, A.; Nicolosi, V.; Coleman, J. N. Scalable Production of Large Quantities of Defect-Free Few-Layer Graphene by Shear Exfoliation in Liquids. *Nat. Mater.* **2014**, *13* (6), 624−630.

(6) Kumar, N.; Salehiyan, R.; Chauke, V.; Joseph Botlhoko, O.; Setshedi, K.; Scriba, M.; Masukume, M.; Sinha Ray, S. Top-down Synthesis of Graphene: A Comprehensive Review. *FlatChem.* **2021**, *27*, 100224.

(7) Luong, D. X.; Bets, K. V.; Algozeeb, W. A.; Stanford, M. G.; Kittrell, C.; Chen, W.; Salvatierra, R. V.; Ren, M.; McHugh, E. A.; Advincula, P. A.; Wang, Z.; Bhatt, M.; Guo, H.; Mancevski, V.; Shahsavari, R.; Yakobson, B. I.; Tour, J. M. Gram-Scale Bottom-up Flash Graphene Synthesis. *Nature* **2020**, *577* (7792), 647−651.

(8) Sun, L.; Yuan, G.; Gao, L.; Yang, J.; Chhowalla, M.; Gharahcheshmeh, M. H.; Gleason, K. K.; Choi, Y. S.; Hong, B. H.; Liu, Z. Chemical Vapour Deposition. *Nature Reviews Methods Primers* **2021**, *1*, 6.

(9) Wu, F.; Huang, R.; Mu, D.; Wu, B.; Chen, Y. Controlled Synthesis of Graphitic Carbon-Encapsulated a-Fe 2 O 3 Nanocomposite via Low-Temperature Catalytic Graphitization of Biomass and Its Lithium Storage Property. *Electrochim. Acta* **2016**, *187*, 508−516.

(10) Thompson, E.; Danks, A. E.; Bourgeois, L.; Schnepp, Z. Iron-Catalyzed Graphitization of Biomass. *Green Chem.* **2015**, *17*, 551.

(11) Franklin, R. Crystallyte Growth in Graphitizing and Non-Graphitizing Carbons. *Proc. R. Soc. A: Math., Phys. Eng. Sci.* **1947**, *71* (6), 196−218.

(12) Thambiliyagodage, C. J.; Ulrich, S.; Araujo, P. T.; Bakker, M. G. Catalytic Graphitization in Nanocast Carbon Monoliths by Iron, Cobalt and Nickel Nanoparticles. *Carbon N Y* **2018**, *134*, 452−463.

(13) Hongbo Du; Deng, F.; Kommalapati, R. R.; Amarasekara, A. S. Iron Based Catalysts in Biomass Processing. *Renewable & Sustainable Energy Reviews* **2020**, *134*, 110292.

(14) Hoekstra, J.; Beale, A. M.; Soulimani, F.; Versluijs-Helder, M.; Van De Kleut, D.; Koelewijn, J. M.; Geus, J. W.; Jenneskens, L. W. The Effect of Iron Catalyzed Graphitization on the Textural Properties of Carbonized Cellulose: Magnetically Separable Graphitic Carbon Bodies for Catalysis and Remediation. *Carbon N Y* **2016**, *107*, 248−260.

(15) Li, H.; Zhang, H.; Li, K.; Zhang, J.; Sun, M.; Su, B. Catalytic Graphitization of Coke Carbon by Iron: Understanding the Evolution of Carbon Structure, Morphology and Lattice Fringes. *Fuel* **2020**, *279*, 118531.

(16) Gomez-Martin, A.; Schnepp, Z.; Ramirez-Rico, J. Structural Evolution in Iron-Catalyzed Graphitization of Hard Carbons. *Chem. Mater.* **2021**, *33* (9), 3087−3097.

(17) Gai, L.; Li, J.; Wang, Q.; Tian, R.; Li, K. Evolution of Biomass to Porous Graphite Carbon by Catalytic Graphitization. *J. Environ. Chem. Eng.* **2021**, *9* (6), 106678.

(18) Maslova, O. A.; Ammar, M. R.; Guimbretière, G.; Rouzaud, J. N.; Simon, P. Determination of Crystallite Size in Polished Graphitized Carbon by Raman Spectroscopy. *Phys. Rev. B Condens Matter Mater. Phys.* **2012**, *86* (13), 1−5.

(19) Muzyka, R.; Drewniak, S.; Pustelny, T.; Chrubasik, M.; Gryglewicz, G. Characterization of Graphite Oxide and Reduced Graphene Oxide Obtained from Different Graphite Precursors and

Oxidized by Different Methods Using Raman Spectroscopy. *Materials* **2018**, *11* (7), 1050.
(20) Bernard, S.; Beyssac, O.; Benzerara, K.; Findling, N.; Tzvetkov, G.; Brown, G. E. XANES, Raman and XRD Study of Anthracene-Based Cokes and Saccharose-Based Chars Submitted to High-Temperature Pyrolysis. *Carbon N Y* **2010**, *48* (9), 2506−2516.
(21) Ferrari, A. C. Raman Spectroscopy of Graphene and Graphite: Disorder, Electron-Phonon Coupling, Doping and Nonadiabatic Effects. *Solid State Commun.* **2007**, *143* (1−2), 47−57.
(22) Ferrari, A. C.; Robertson, J. Raman Spectroscopy of Amorphous, Nanostructured, Diamond-like Carbon, and Nanodiamond. *Philosophica Transactions* **2004**, *362* (1824), 2477−2512.
(23) Pawlyta, M.; Rouzaud, J. N.; Duber, S. Raman Microspectroscopy Characterization of Carbon Blacks: Spectral Analysis and Structural Information. *Carbon N Y* **2015**, *84* (1), 479−490.
(24) Mallet-Ladeira, P.; Puech, P.; Weisbecker, P.; Vignoles, G. L.; Monthioux, M. Behavior of Raman D Band for Pyrocarbons with Crystallite Size in the 2−5 Nm Range. *Appl. Phys. A Mater. Sci. Process* **2014**, *114* (3), 759−763.
(25) Ferrari, A.; Robertson, J. Interpretation of Raman Spectra of Disordered and Amorphous Carbon. *Phys. Rev. B Condens Matter Mater. Phys.* **2000**, *61* (20), 14095−14107.
(26) Pimenta, M. A.; Dresselhaus, G.; Dresselhaus, M. S.; Cançado, L. G.; Jorio, A.; Saito, R. Studying Disorder in Graphite-Based Systems by Raman Spectroscopy. *Phys. Chem. Chem. Phys.* **2007**, *9* (11), 1276−1291.
(27) Schuepfer, D. B.; Badaczewski, F.; Guerra-Castro, J. M.; Hofmann, D. M.; Heiliger, C.; Smarsly, B.; Klar, P. J. Assessing the Structural Properties of Graphitic and Non-Graphitic Carbons by Raman Spectroscopy. *Carbon N Y* **2020**, *161*, 359−372.
(28) Zickler, G. A.; Smarsly, B.; Gierlinger, N.; Peterlik, H.; Paris, O. A Reconsideration of the Relationship between the Crystallite Size La of Carbons Determined by X-Ray Diffraction and Raman Spectroscopy. *Carbon N Y* **2006**, *44* (15), 3239−3246.
(29) Tuinstra, F.; Koenig, J. Raman Spectrum of Graphite. *J. Chem. Phys.* **1970**, *53* (3), 1126−1130.
(30) Knight, D. S.; White, W. B. Characterization of Diamond Films by Raman Spectroscopy. *J. Mater. Res.* **1989**, *4* (2), 385−393.
(31) Cançado, L. G.; Takai, K.; Enoki, T.; Endo, M.; Kim, Y. A.; Mizusaki, H.; Speziali, N. L.; Jorio, A.; Pimenta, M. A. Measuring the Degree of Stacking Order in Graphite by Raman Spectroscopy. *Carbon N Y* **2008**, *46*, 272−275.
(32) Caṇado, L. G.; Takai, K.; Enoki, T.; Endo, M.; Kim, Y. A.; Mizusaki, H.; Jorio, A.; Coelho, L. N.; Magalhães-Paniago, R.; Pimenta, M. A. General Equation for the Determination of the Crystallite Size La of Nanographite by Raman Spectroscopy. *Appl. Phys. Lett.* **2006**, *88* (16), 163106.
(33) Mallet-Ladeira, P.; Puech, P.; Toulouse, C.; Cazayous, M.; Ratel-Ramond, N.; Weisbecker, P.; Vignoles, G. L.; Monthioux, M. A Raman Study to Obtain Crystallite Size of Carbon Materials: A Better Alternative to the Tuinstra-Koenig Law. *Carbon N Y* **2014**, *80* (1), 629−639.
(34) Alexander, L.; Klug, H. P. Determination of Crystallite Size with the X-Ray Spectrometer. *J. Appl. Phys.* **1950**, *21* (2), 137−142.
(35) Malard, L. M.; Pimenta, M. A.; Dresselhaus, G.; Dresselhaus, M. S. Raman Spectroscopy in Graphene. *Phys. Rep.* **2009**, *473* (5−6), 51−87.
(36) Dresselhaus, M. S.; Jorio, A.; Hofmann, M.; Dresselhaus, G.; Saito, R. Perspectives on Carbon Nanotubes and Graphene Raman Spectroscopy. *Nano Lett.* **2010**, *10* (3), 751−758.
(37) Neeli, S. T.; Ramsurn, H. Synthesis and Formation Mechanism of Iron Nanoparticles in Graphitized Carbon Matrix Using Biochar from Biomass Model Compounds as a Support. *Carbon N Y* **2018**, *134*, 480−490.
(38) Sevilla, M.; Fuertes, A. B. Graphitic Carbon Nanostructures from Cellulose. *Chem. Phys. Lett.* **2010**, *490* (1−3), 63−68.
(39) Carvill, J. *Mechanical Engineer's Data Handbook*; Elsevier Science Publishers B.V.: 2003.
(40) Hoekstra, J.; Beale, A. M.; Soulimani, F.; Versluijs-Helder, M.; Geus, J. W.; Jenneskens, L. W. Base Metal Catalyzed Graphitization of Cellulose: A Combined Raman Spectroscopy, Temperature-Dependent X-Ray Diffraction and High-Resolution Transmission Electron Microscopy Study. *J. Phys. Chem. C* **2015**, *119*, 10653−10661.
(41) Egami, T.; Billinge; Simon, J. L. *Underneath the Bragg Peaks: Structural Analysis of Complex Materials*; Pergamon: Elmsford, NY, 2003.
(42) Poulain, A.; Dupont, C.; Martinez, P.; Guizani, C.; Drnec, J. Wide-Angle X-Ray Scattering Combined with Pair Distribution Function Analysis of Pyrolyzed Wood. *J. Appl. Crystallogr.* **2019**, *52* (iii), 60−71.
(43) Sadezky, A.; Muckenhuber, H.; Grothe, H.; Niessner, R.; Pöschl, U. Raman Microspectroscopy of Soot and Related Carbonaceous Materials: Spectral Analysis and Structural Information. *Carbon N Y* **2005**, *43*, 1731−1742.
(44) Vollebregt, S.; Ishihara, R.; Tichelaar, F. D.; Hou, Y.; Beenakker, C. I. M. Influence of the Growth Temperature on the First and Second-Order Raman Band Ratios and Widths of Carbon Nanotubes and Fibers. *Carbon N Y* **2012**, *50* (10), 3542−3554.
(45) Weisbecker, P.; Leyssale, J.-M. Carbones Pyrolytiques Ou Pyrocarbones : Des Matériaux Multiéchelles et Multiperformances. *Techniques de l'Ingénieur* **2015**, *NM3150*, 1−25.
(46) Balzar, D. X-Ray Diffraction Line Broadening: Modeling and Applications to High-Tc Superconductors. *J. Res. Natl. Inst Stand Technol.* **1993**, *98* (3), 321.
(47) *Powder Diffraction. Theory and Practice*; Dinnebier, R. E., Billinge, S. J. L., Eds.; RSC Publishing: 2008.
(48) Uvarov, V.; Popov, I. Metrological Characterization of X-Ray Diffraction Methods at Different Acquisition Geometries for Determination of Crystallite Size in Nano-Scale Materials. *Mater. Charact* **2013**, *85*, 111−123.
(49) Toby, B. H.; Von Dreele, R. B. GSAS-II: The Genesis of a Modern Open-Source All Purpose Crystallography Software Package. *J. Appl. Crystallogr.* **2013**, *46* (2), 544−549.
(50) Qiu, X.; Thompson, J. W.; Billinge, S. J. L. PDFgetX2: A GUI-Driven Program to Obtain the Pair Distribution Function from X-Ray Powder Diffraction Data. *J. Appl. Crystallogr.* **2004**, *37* (4), 678.
(51) Farrow, C. L.; Juhas, P.; Liu, J. W.; Bryndin, D.; Božin, E. S.; Bloch, J.; Proffen, T.; Billinge, S. J. L. PDFfit2 and PDFgui: Computer Programs for Studying Nanostructure in Crystals. *J. Phys.: Condens. Matter* **2007**, *19* (33), 335219.
(52) White, C. E.; Daemen, L. L.; Hartl, M.; Page, K. Intrinsic Differences in Atomic Ordering of Calcium (Alumino)Silicate Hydrates in Conventional and Alkali-Activated Cements. *Cem. Concr. Res.* **2015**, *67*, 66−73.
(53) Morandeau, A. E.; White, C. E. In Situ X-Ray Pair Distribution Function Analysis of Accelerated Carbonation of a Synthetic Calcium-Silicate-Hydrate Gel. *J. Mater. Chem. A Mater.* **2015**, *3* (16), 8597−8605.
(54) Jurkiewicz, K.; Duber, S.; Fischer, H. E.; Burian, A. Modelling of Glass-like Carbon Structure and Its Experimental Verification by Neutron and X-Ray Diffraction. *J. Appl. Crystallogr.* **2017**, *50* (1), 36−48.